Beyond Ohm's law: Bernoulli effect and streaming in electron hydrodynamics

Aaron Hui [●],[1] Vadim Oganesyan,[2,3] and Eun-Ah Kim[4]

[1]*School of Applied & Engineering Physics, Cornell University, Ithaca, New York 14853, USA*
[2]*Department of Physics and Astronomy, College of Staten Island, CUNY, Staten Island, New York 10314, USA*
[3]*Physics Program and Initiative for the Theoretical Sciences, The Graduate Center, CUNY, New York, New York 10016, USA*
[4]*Department of Physics, Cornell University, Ithaca, New York 14853, USA*

Recent observations of nonlocal transport in ultraclean two-dimensional materials raised the tantalizing possibility of accessing hydrodynamic correlated transport of a many-electron state. However, it has been pointed out that nonlocal transport can also arise from impurity scattering rather than interaction. At the crux of the ambiguity is the focus on linear effects, i.e., Ohm's law, which cannot easily differentiate among different modes of transport. Here we propose experiments that can reveal rich hydrodynamic features in the system by tapping into the nonlinearity of the Navier-Stokes equation. Three experiments we propose will each manifest a unique phenomenon that is well known in classical fluids: the Bernoulli effect, Eckart streaming, and Rayleigh streaming. Analysis of known parameters confirms that the proposed experiments are feasible and the hydrodynamic signatures are within reach of graphene-based devices. Experimental realization of any one of the three phenomena will provide a stepping stone to formulating and exploring the notions of nonlinear electron fluid dynamics with an eye to celebrated examples from classical nonlaminar flows, e.g., pattern formation and turbulence.

I. INTRODUCTION

Electron hydrodynamics offers a powerful framework to understand transport in strongly correlated electron systems [1–16]. The pursuit of electron hydrodynamics gained new impetus with the advent of recent experiments in a number of ultraclean two-dimensional (2D) materials [17–26] making a case for electron hydrodynamics through observations of nonlocal transport, consistent with viscous flows familiar in classical fluids. Such observations as vortices, Poiseuille-like flow profiles, and unconventional channel width dependencies of resistance are indeed consistent with viscous effects in a linearized Navier-Stokes equation. However, these results are all in the linear-response regime, and they can be ultimately described using a nonlocal variant of Ohm's law. Indeed, the linearized Navier-Stokes equation can be simply recast using a nonlocal conductivity $\sigma(q)$ [27–29]. While nonlocal transport can certainly be couched in the formalism of hydrodynamics, it is also clear that inherently finite length scales of a realistic fermionic system can conspire to produce nonlocal transport indistinguishable from that implied by the Navier-Stokes equation [29]. Other ways of accessing electron hydrodynamics are of great interest as we seek to understand and isolate competing effects.

The overarching goal of this paper is to highlight the existence of nonlinear electron *phenomena* that may be associated with an effective hydrodynamic description. With that in mind, we adapt the Navier-Stokes (NS) equations of classical fluid dynamics by introducing momentum relaxation and Coulomb effects to make the discussion of the electron phenomenology explicit. We do not tackle the important and difficult question of a proper microscopic derivation of NS—indeed, there is evidence that many available electron devices are not quite in the asymptotic hydrodynamic regime [30,31]. We do, however, find strong evidence in known material and device parameters to support the feasibility of our proposals. It is worth emphasizing that while the phenomena we focus on in this work are leading deviations from linear response, the NS results we obtain also suggest the presence of instabilities at finite nonlinearity. As in traditional classical hydrodynamics, these different regimes are naturally demarcated using dimensionless Reynolds numbers.

In Fig. 1, we summarize the three proposals that we discuss in this paper. The rest of the paper is organized as follows. Section II sets up the notation and formalism of NS, paying particular attention to the spectrum of Reynolds numbers required to quantify nonlinear phenomena. Here, we also collect Reynolds number estimates from known parameters for graphene. Section III focuses on the manifestation of the Bernoulli effect in the nonlinear current-voltage response of an electron funnel. Section IV derives the generation of downconverted dc current from a localized finite-frequency excitation, analogous to Eckart streaming or "quartz wind." Section V describes the generation of static electron vortices (akin to Rayleigh streaming) from an extended ac excitation. Sections II–V are accompanied by Appendixes A–D containing complete details of calculations. Finally, we close with a summary of results and a discussion of open problems, including the role of interactions.
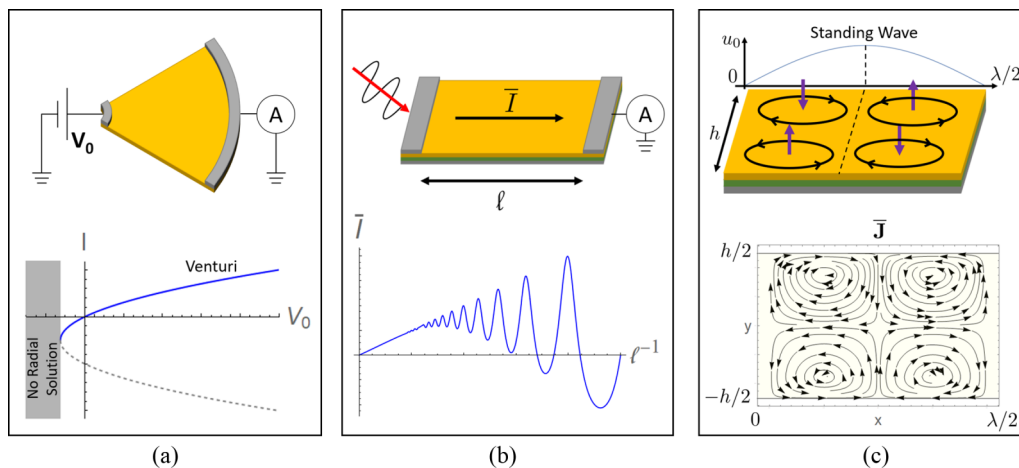
FIG. 1. Proposed experimental setups and sketches of their observed effects. (a) The Venturi geometry, comprised of a circular wedge of the hydrodynamic material in yellow. A nonlinear I-V characteristic with $I \sim \sqrt{V_0}$ behavior is expected, marked in blue. The gray dashed line represents an unstable solution branch, while the gray region represents a possible instability toward turbulent and/or intermittent flow. (b) Eckart streaming. A voltage oscillation of zero mean is driven on one side of a back-gated device, leading to a rectified dc current $\bar{I}$. For large l, the dc current scales as l^{-1}. For small l, oscillations due to interference with the reflected wave become visible. (c) Rayleigh streaming. In a similar back-gated geometry of (b), a standing wave of current oscillations of amplitude u_0 and of period λ along x is imposed, leading to an oscillating magnetic field pattern of period $\lambda/2$ along x. These magnetic fields arise due to the formation of vortical current cells of size $\lambda/4$ along x and $h/2$ along y, shown in the lower panel.

II. FORMALISM AND PARAMETERS

A. Equations of fluid dynamics

The hydrodynamics of an electron fluid, as a long-wavelength effective theory, is described by a set of conservation laws for variables that decay slowly compared to the coarse-graining scale of the system. Although Galilean invariance is not microscopically present in electronic materials (e.g., graphene), the Navier-Stokes equation has been derived from kinetic theory when momentum-relaxing processes are weak [32–34]. The momentum (Navier-Stokes) and density continuity equations, which will be our primary interest in this paper, are [35]

$$\frac{\partial n}{\partial t} + \boldsymbol{\nabla} \cdot (n\mathbf{v}) = \mathbf{0}, \tag{1}$$

$$\frac{\partial (\rho \mathbf{v})}{\partial t} = \mathbf{F}_{\text{conv}} - \boldsymbol{\nabla} p - \rho_e \boldsymbol{\nabla} \phi$$
$$+ \left[\frac{4}{D}\nu + \tilde{\zeta}\right] \rho \boldsymbol{\nabla} \boldsymbol{\nabla} \cdot \mathbf{v} - \rho \nu \boldsymbol{\nabla} \times \boldsymbol{\nabla} \times \mathbf{v} - \rho \gamma \mathbf{v}, \tag{2}$$

$$\mathbf{F}_{\text{conv}} \equiv -\boldsymbol{\nabla} \cdot (\rho \mathbf{v} \otimes \mathbf{v}) = -\rho \mathbf{v} \cdot \boldsymbol{\nabla} \mathbf{v} - \mathbf{v} \boldsymbol{\nabla} \cdot (\rho \mathbf{v}), \tag{3}$$

where $\mathbf{v}$ is the velocity field, n is the number density field with mass m and charge e (ρ and ρ_e are the mass and charge densities, respectively), ν and $\tilde{\zeta}$ are the kinematic shear and bulk viscosities, respectively, and we will be working in dimension $D = 2$ [36]. For graphene specifically, we remark that there are quantitative corrections to Eq. (2) (see Ref. [32]). In particular, the hydrodynamic mass m is not the quasiparticle mass in the case of graphene, but is an effective mass related to the local energy density $m \sim \epsilon/v_F^2$. Moreover, there is a multiplicative correction to the convective term. We will approximate m as a constant and ignore this multiplicative correction, which we justify in Sec. II B. The convective term

$\mathbf{F}_{\text{conv}}$ is written to emphasize that it acts as an effective force; this will be the primary source of nonlinear behavior. The remaining terms may also be thought of as (generalized) forces, and we can take their ratios for a particular flow pattern to characterize their relative importance. In addition to the conventional "viscous" Reynolds number Re_ν corresponding to shear dissipation, a momentum-relaxation Reynolds number Re_γ will be of interest. For simple nonsingular flow profiles, these may be expressed as

$$\text{Re}_\nu \equiv \frac{\boldsymbol{\nabla} \cdot (\rho \mathbf{v} \otimes \mathbf{v})}{\rho \nu \nabla^2 \mathbf{v}} = \frac{vL}{\nu} = \frac{IL}{\rho_e h \nu}, \tag{4}$$

$$\text{Re}_\gamma \equiv \frac{\boldsymbol{\nabla} \cdot (\rho \mathbf{v} \otimes \mathbf{v})}{\rho \gamma \mathbf{v}} = \frac{v}{L\gamma} = \frac{I}{\rho_e h L \gamma}, \tag{5}$$

with the help of characteristic velocity v, gradient $1/L$, channel width h, and net current $I = \rho_e h v$. In this paper, we primarily focus on the limit of low Reynolds numbers $\text{Re}_\gamma, \text{Re}_\nu \ll 1$, i.e., leading corrections to linear response [37].

Following standard practice, we make a further assumption of local equilibrium to write equations of state for p and ϕ, which closes the set of continuity equations above. We take a back-gated geometry as shown in Fig. 1(b), where the hydrodynamic metal and the back-gate separated by a distance d have a capacitance per unit area $C = \frac{\epsilon \epsilon_0}{d}$. Therefore, we take the following local relationships:

$$p = s_{\text{FL}}^2 \rho, \tag{6}$$

$$\phi = \rho_e / C, \tag{7}$$

where s_{FL} is a constant corresponding to the speed of sound in an uncharged, undamped fluid (i.e., a Fermi liquid). In Eq. (7), also called the "gradual channel approximation," the long-range Coulomb tail is screened by the gate so that the

longitudinal dispersion is gapless. This approximation is valid when the distance d between the hydrodynamic metal and the gate is much smaller than the typical wavelength of oscillations [33,38,39]. Therefore, both p and ϕ obey the same functional form; if the density $\rho = \rho^{(0)}$ is constant, p can be absorbed into an effective voltage $\phi_{\text{eff}} \equiv \phi + \frac{p}{\rho_e^{(0)}}$ in the momentum equation. In particular, as a result of Eq. (7) there is also an electronic contribution $s_{\text{cap}}^2 = \frac{n^{(0)}e^2}{Cm}$ to the undamped speed of sound $s_0 \equiv \sqrt{s_{\text{FL}}^2 + s_{\text{cap}}^2}$.

B. Parameter estimates

To estimate parameters, as a model system we consider a graphene-hBN stack with gate-channel separation $d = 100$ nm and average carrier density $n^{(0)} \sim 10^{12}$ cm^{-2} tuned away from charge neutrality so that we can consider a single band. In graphene, the relaxation rate $\gamma \sim 650$ GHz and $\nu \sim 0.1$ m^2/s [18], so that the viscous length scale $r_d = \sqrt{\frac{\nu}{\gamma}} \sim 0.4$ μm [29]. We will also take $\tilde{\zeta} \sim 0$ [40,41]. The relative dielectric constant of hBN is $\epsilon \sim 3.9$ [39,42], and we approximate m and e to be the bare electron mass and charge, respectively. Therefore, the electronic contribution to sound is $s_{\text{cap}} \sim 0.9 \times 10^6$ m/s. The speed of sound of Fermi liquids is $s_{\text{FL}} \sim v_F$ [43], and Fermi velocities for metals are generally $v_F \sim 10^6$ m/s [44]. Therefore, we will approximate the undamped speed of sound $s_0 \sim 2 \times 10^6$ m/s. Using the dispersion relation in Eq. (A1), for $\omega = 1$ THz we have the true speed of sound $s \sim 1.9 \times 10^6$ m/s and attenuation coefficient $\alpha \sim 1/(6 \, \mu\text{m})$. As a rough estimate, for characteristic lengths $h \sim L \sim 5$ μm the Reynolds numbers are $\text{Re}_\nu \sim I/(160 \, \mu\text{A})$ and $\text{Re}_\gamma \sim I/(26 \, \text{mA})$. The ratio $\text{Re}_\nu / \text{Re}_\gamma \sim L^2/r_d^2$ is controlled by the viscous length scale $r_d \sim 0.4$ μm, so current micrometer-scale experiments will be in a regime where Re_γ tends to dominate the nonlinear behavior. We remark that the apparent paradox that hydrodynamic effects could be dominated by momentum relaxation is due to linear-response considerations; by tuning the sample width h such that $r_d \ll h$, a hydrodynamic description of the material remains valid but becomes indistinguishable from Ohm's law in the absence of convection.

We now justify our assumptions of m constant and convective correction ξ negligible for the case of graphene. As shown in Ref. [32], the mass fluctuations $\delta m \sim m_0[O(\delta n/T) + O(u^2/v_F^2)]$. For our parameters, operating at currents $I \sim 100$ μA and channel widths $h \sim 5$ μm at room temperature $T = 300$ K, the corrections $\delta m \sim 0.01m$ and are perturbatively small. Keeping any new nonlinearities introduced by δm up to second-order, we find that it only introduces quantitative $O(1)$ corrections to the dissipative terms γ, ν, and $\bar{\zeta}$. Therefore, m constant is valid at our level of approximation. For the multiplicative correction to convection, for our parameters where $\mu/T \gtrsim 1$ the multiplicative factor is roughly $1/4$; this is only an $O(1)$ quantitative correction, and it is valid to ignore it at our level of approximation.

III. ELECTRONIC BERNOULLI EFFECT

We now apply the hydrodynamic formalism to derive a nonlinear contribution to the I-V characteristic $V \propto I^2$ in what
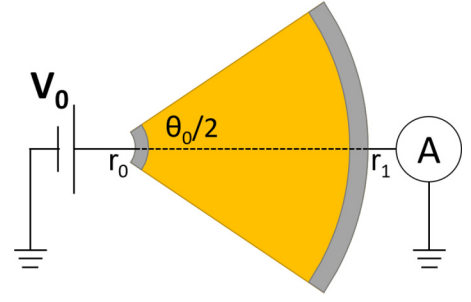

FIG. 2. A top view of the Venturi geometry, with inner radius r_0, outer radius r_1, and total wedge angle θ_0.

we call the "Venturi" geometry (see Fig. 2), first analytically in the limit $\nu \to 0$. For boundary conditions, we fix the voltage $\phi(r_0) = V_0$ and $\phi(r_1) = 0$ and take no-slip (vanishing velocity) at the side walls $\theta = \pm\theta_0/2$. We find that the stationary purely radial "plug flow" ansatz $\mathbf{v} = v_r(r)\Theta(\theta_0^2 - 4\theta^2)\hat{\mathbf{r}}$ is a solution (with Θ the Heaviside step-function). The absence of viscosity is crucial as it allows for a zero-thickness boundary layer in this highly symmetric flow [45]. The Navier-Stokes equation [Eq. (2)] reduces to a simple ordinary differential equation

$$\frac{\partial}{\partial r}\left[e\phi + \frac{1}{2}mv_r^2 \right] + m\gamma v_r = 0, \qquad (8)$$

where we have subsumed pressure into ϕ for simplicity [46]. We further take the divergence-free ("incompressible flow") ansatz $v_r = \frac{I}{\rho_e^{(0)}\theta_0}\frac{1}{r}$, where the yet-undetermined constant I is the total current and $\rho_e^{(0)}$ is the average charge density. Substituting this ansatz into Eq. (8) and integrating from r_0 to r_1 (see Fig. 2), we obtain the nonlinear I-V characteristic

$$V_0 = \frac{1}{\sigma_D}\left[\frac{l\ln(h_1/h_0)}{h_1 - h_0}I - \frac{1}{2}\left(\frac{1}{h_0^2} - \frac{1}{h_1^2} \right)\frac{I^2}{\rho_e\gamma} \right], \qquad (9)$$

where $\sigma_D = \frac{n^{(0)}e^2}{m\gamma}$ is the Drude conductivity, $l = r_1 - r_0$ is the length, and $h_0 = \theta_0 r_0$ and $h_1 = \theta_0 r_1$ are the widths at the contacts. The first term on the right-hand side corresponds to the Ohmic contribution, while the second term is the nonlinear I^2 contribution from convection. We emphasize that the nonlinear contribution is strongly geometric, vanishing for typical rectangular geometries [47] where $h_0 = h_1$. To further isolate the nonlinearity, we exploit the parity difference between the two contributions. Because the nonlinearity is of even parity, a nonzero symmetrized current $I_{\text{sym}}(V_0) \equiv \frac{1}{2}[I(V_0) + I(-V_0)]$ provides a direct signature of the nonlinearity. To estimate this effect, in Fig. 3 we plot in blue the current fraction I_{sym}/I and the I-V characteristic of Eq. (9) for wedge angle $\theta_0 = \pi/2$ with $r_0 = 5$ μm, $r_1 = 10$ μm, and graphene-hBN parameters as discussed in Sec. II B. To incorporate a finite shear viscosity, which is difficult to solve analytically (see Appendix B), we solve the Navier-Stokes equations numerically and plot the results as points in Fig. 1(a). The exact ($\nu = 0$) result of Eq. (9) matches well with the numerical result, as expected because the viscous length scale $r_d \equiv \sqrt{\frac{\nu}{\gamma}} \ll r_0\theta_0$ is small for experimentally relevant parameters. As demon-
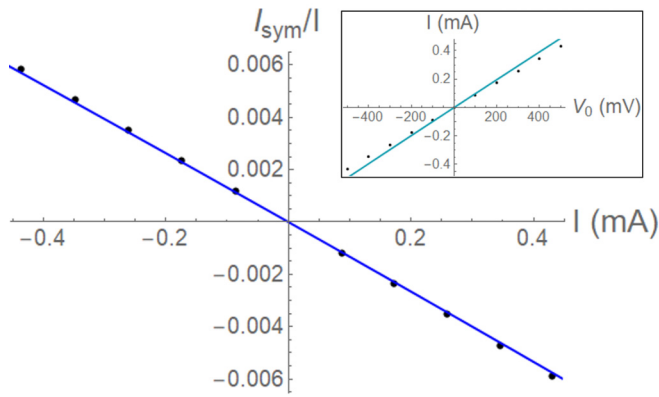
FIG. 3. Main: a parametric plot of the voltage-symmetrized current $I_{\text{sym}}(V_0) \equiv \frac{1}{2}[I(V_0) + I(-V_0)]$ against total current $I(V_0)$. Inset: the I-V characteristic. The solid lines are obtained analytically from Eq. (9) in the $\nu \to 0$ limit, and the points are obtained numerically with finite ν. Fixed-voltage boundary conditions are taken. The inner and outer radii are 5 and 10 μm, respectively, with wedge angle $\theta_0 = \pi/2$, with graphene parameters $\nu = 0.1$ m^2/s and $\gamma = 650$ GHz. Since $r_d \sim 0.4$ μm and lengths are ~ 10 μm, viscous corrections to the analytic $\nu \to 0$ solution should be $\sim 5\%$.

strated by Fig. 1(a), this nonlinear effect ($I_{\text{sym}} \sim 400$ nA for $I \sim 200$ μA) should be experimentally measurable.

This nonlinear I-V characteristic in electronic hydrodynamics is the analog of the Bernoulli effect in classical hydrodynamics, the prototypical example of convective acceleration, which is traditionally demonstrated using a Venturi tube. The Bernoulli effect is typically demonstrated in an inviscid fluid of divergence-free (incompressible) flow, analogous to our assumptions. In fact, the classical Bernoulli (energy conservation) equation is analogous to Eq. (8); the term in brackets corresponds to the classical Bernoulli contribution (i.e., when $\gamma = 0$), while the γ term accounts for the additional dissipation from a finite conductivity. As a result, the nonlinear term of the I-V characteristic Eq. (9) can be calculated exactly by classical Bernoulli considerations.

We turn to the subtle issue of solving for the total current $I(V_0)$ given the input voltage V_0, i.e., verifying that the ansatz satisfies the boundary conditions. Because this requires solving a quadratic equation for I, the solution is generically multivalued and may not even have a solution. In the limit of small V_0, linear response must provide the correct answer on physical grounds; this selects the solution branch continuously connected to the solution $I = 0$ at $V_0 = 0$, where parity was broken by γ. The opposite branch is therefore expected to be unstable to θ-dependent perturbations. The region where the purely radial solution does not exist corresponds to particle flow in the divergent direction; for classical fluids, it is known that divergent flow eventually becomes unstable and develops turbulence [48,49]. To estimate the scale of nonlinearity at which the radial ansatz fails, one can define a Reynolds number

$$\text{Re}_\gamma \equiv \frac{\int_{r_0}^{r_1} dr F_{\text{conv},r}}{-\int_{r_0}^{r_1} dr \rho \gamma v_r} = \frac{-1}{2lh_0} \frac{I}{\rho_e \gamma} \left[\frac{\frac{h_1}{h_0} - 1}{\ln \frac{h_1}{h_0}} \left(1 - \frac{h_0^2}{h_1^2} \right) \right],$$

(10)

which is precisely the ratio of the two terms in Eq. (9). The instability point occurs at $\text{Re}_\gamma = -1/2$. We summarize the resolution of these subtleties in Fig. 1(a).

Finally, we now highlight three aspects of the Bernoulli nonlinearity that should help identify it unambiguously in experiments. To start, following Eq. (9) we note that the quadratic term is independent of the momentum relaxation parameter γ, and hence may be identified by comparing I-V traces taken at different temperatures or even from different samples of the same material. Secondly, the simple charge-density dependence may be probed by varying back-gate voltage. After factoring out the density-dependent Drude resistivity $1/\sigma_D$ [cf. Eq. (9)], the nonlinear term only has an inverse dependence on charge density (and its sign depends on the carrier charge). Lastly, Eq. (9) has a distinct geometric dependence interpolating in a somewhat unusual way between conventional and ballistic transport. For fixed aspect ratios h_1/h_0 and l/h_0, we find that the Ohmic resistance contribution scales with the size of the device as $1/h_0$ while the nonlinear Bernoulli contribution scales as $1/h_0^2$. In addition, the Ohmic resistance contribution has conventional linear scaling with length l, while the nonlinear Bernoulli contribution has the l-independent hallmark of *ballistic* transport. This effect, therefore, stands apart from generic nonlinearities, which are expected to be inversion-odd when the crystal structure is inversion-symmetric (e.g., in graphene), and from Joule heating effects, which would also provide inversion-odd nonlinearities and would not have the l-independent ballistic scaling.

IV. ECKART STREAMING: A "HYDRODYNAMIC SOLAR CELL"

A dramatic effect of nonlinearity occurs upon applying an oscillatory drive: down-conversion. In a back-gated device of length l and width h [see Fig. 1(b)], we consider setting up a traveling longitudinal (sound) wave by application of a voltage oscillation $\phi(x = 0) = V_0 \cos \omega t$ at the left contact with the right contact grounded [$\phi(x = l) = 0$]. This will result in a dc current via the down-conversion sourced by the convective force [Eq. (3)]. Such a device can be described as a "hydrodynamic solar cell" providing a dc photocurrent if the (localized) voltage oscillation is driven by EM radiation. For simplicity, we will focus on bulk dissipation (i.e., attenuation due to $\alpha > 0$) contributions to the convective force and neglect those of boundary dissipation, which only results in a quantitative underestimate of the dc current (see Appendix C 5). This is the electronic analog of Eckart streaming in classical hydrodynamics, where the convective force is primarily generated by bulk dissipation [50–53]. To see this, we need to solve the full Navier-Stokes equation [Eq. (2)], whose nonlinearity precludes a single-mode ansatz. To handle this, we will seek a perturbative solution in the input voltage amplitude V_0 (see Appendix C for full mathematical details).

A. Perturbative calculation

We begin by expanding the hydrodynamic variables in a power series expansion of V_0, e.g., $\rho = \rho^{(0)} + \rho^{(1)} + \rho^{(2)} + \cdots$; $\rho^{(0)}$ corresponds to the equilibrium mass density, while

$\rho^{(1)}$ and $\rho^{(2)}$ are the first- and second-order solutions. At leading (linear) order, the single-mode ansatz $\phi^{(1)} \sim V_0 e^{i(\pm k_l x - \omega t)}$ along x with wave number $k_l = k + i\alpha$ is appropriate. Imposing the fixed-voltage boundary conditions, the solution of $\phi^{(1)}$ is a traveling wave with a reflected component; the grounded edge acts as a mirror. Because of the back-gate providing a capacitance per area C, the voltage oscillation of amplitude V_0 sets up a charge-density oscillation $\rho_e^{(1)} = C\phi^{(1)}$ of amplitude CV_0 [see Eq. (7)]. Via the density continuity equation [Eq. (1)], the density oscillations drive a longitudinal velocity oscillation $v_x^{(1)}$, schematically written as

$$v_x^{(1)} \sim u_0 \text{Re}[e^{(ik-\alpha)x - i\omega t} + e^{(ik-\alpha)(2l-x) - i\omega t}], \qquad (11)$$

where Re denotes the real part and $u_0 = \frac{CV_0}{\rho_e^{(0)}} \frac{\omega}{|k_l|}$ is the velocity amplitude. We also take a no-slip boundary condition, which is *not* satisfied by $v_x^{(1)}$. However, as previously stated, we will neglect the boundary corrections to $v_x^{(1)}$ for simplicity (see Appendix C 5) [54]. As a result, the leading-order solution $v_x^{(1)}$ results in a dc convective force [see Eq. (3)]

$$\overline{F_{\text{conv},x}^{(2)}} = \rho^{(0)} u_0^2 \frac{\alpha \sinh[2\alpha(l-x)] - k \sin[2k(l-x)]}{\cosh 2\alpha l - \cos 2kl}, \quad (12)$$

where the overbar denotes time-average. The first term in the numerator arises from the bulk dissipation α, while the second term arises from interference effects; in the limit $\alpha l \gg 1$, where interference effects are small, the right-hand side of Eq. (12) simplifies to $\alpha e^{-2\alpha x}$. This rectified dc force will result in a dc current.

We now solve for the second-order dc current $\overline{I^{(2)}}$. The dc current density $\overline{\mathbf{J}^{(2)}} \equiv \rho_e^{(0)} \overline{\mathbf{v}^{(2)}} + \overline{\rho_e^{(1)} \mathbf{v}^{(1)}}$ must be divergence-free to satisfy current conservation [i.e., density continuity Eq. (1)]. With the ansatz $\overline{v_y^{(2)}} = 0$, this implies that the current density $\overline{\mathbf{J}^{(2)}} = \overline{J_x^{(2)}}(y)\hat{\mathbf{x}}$ only varies along y. However, the convective force given by Eq. (12) varies along x. This paradox is resolved by static screening, where the x-dependence of convection will be canceled by contributions from the effective voltage $\overline{\phi_{\text{eff}}^{(2)}} \equiv \overline{\phi^{(2)}} + \frac{1}{\rho^{(0)}} \overline{p^{(2)}}$. Utilizing separation of variables in the NS equation [Eq. (2)], we can solve for $\overline{\phi_{\text{eff}}^{(2)}}$ by applying the voltage-fixed boundary conditions $\overline{\phi^{(2)}}(x=0) = \overline{\phi^{(2)}}(x=l) = 0$. Therefore, the "screened" convective force (which is no longer spatially dependent) becomes

$$\overline{F_{\text{conv},x}^{(2)}} - \rho_e^{(0)} \frac{\partial \overline{\phi_{\text{eff}}^{(2)}}}{\partial x} = \frac{1}{l} \int_0^l dx \overline{F_{\text{conv}}^{(2)}}. \qquad (13)$$

Solving NS for the current density $\overline{J_x^{(2)}}$ and integrating across the channel to get the total current $\overline{I^{(2)}}$, we get

$$\overline{I^{(2)}} = \frac{I_0^2}{\rho_e^{(0)} h} \frac{1}{2l\gamma} \left[1 - \frac{2 - 2\cos 2kl}{\cosh 2\alpha l - \cos 2kl} \right]$$
$$\times \left(1 - \frac{2r_d}{h} \tanh \frac{h}{2r_d} \right), \qquad (14)$$

where $I_0 \equiv \rho_e^{(0)} h u_0$ is the input current amplitude, and we have assumed that convection provides the dominant dc force (see Appendix C 3). The term in parentheses is a viscous correction, reflecting the y-dependence of the current flow
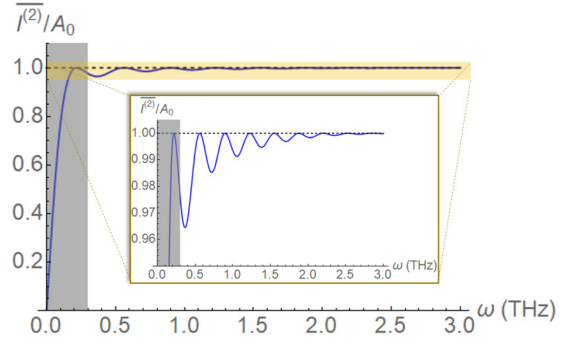

FIG. 4. Main: A plot of $\overline{I^{(2)}}$ at fixed input current amplitude I_0 for device length $l = 30\,\mu$m and graphene-hBN parameters stated in Sec. II B, in units of $A_0 = \frac{I_0^2}{\rho_e^{(0)} h} \frac{1}{2l\gamma} (1 - \frac{2r_d}{h} \tanh \frac{h}{2r_d})$. We remark that this is also a scaled plot of the Reynolds number Re_γ. Inset: a blowup of the yellow highlighted portion. At high frequencies, Re_γ saturates to a constant $A_0 = \frac{I_0}{\rho_e^{(0)} h} \frac{1}{2l\gamma}$, while at sufficiently low frequencies the interference oscillations become more visible. The gray box demarcates the low-frequency region $\omega \ll \gamma$, where perturbation theory in V_0 breaks down for a fixed I_0.

due to no-slip [55]. The bracketed terms correspond to dissipation and interference contributions from the convective force [Eq. (3)], respectively. The effect of these contributions is demonstrated in Fig. 1(b), where we have schematically plotted the dependence of dc current on the channel length l. In the limit $\alpha l \ll 1$, the interference term dominates, leading to oscillatory behavior controlled by kl. In the opposite limit $\alpha l \gg 1$, the interference term becomes negligible, and the dc current scales as $\overline{I^{(2)}} \sim l^{-1}$. Other than the device length l, one could also study the frequency dependence of Eq. (14) [via $k_l(\omega) = k + i\alpha$], which is plotted in Fig. 4 for a fixed I_0 [56]. Similarly, interference effects appear at low frequencies and become negligible at high frequencies.

B. Discussion and estimates

An effect similar to Eckart streaming was previously discussed by Dyakonov and Shur [57] and extended in Ref. [39]. They envisaged operating with zero dc current bias $\overline{I} = 0$ instead of zero dc voltage drop, so that one generates a dc voltage instead of a dc current. These theoretical treatments [39,57] similarly neglected boundary dissipation, which only leads to quantitative corrections to dc voltage. However, for their case, boundary dissipation leads to qualitative flow corrections (see Appendix C 5); further discussion is deferred to Sec. V. We point out that, in either case, if the voltage oscillation is driven by an impingent EM wave, the device is a "hydrodynamic solar cell" generating a dc photocurrent (photovoltage). In contrast to typical solar cells (e.g., a p-n junction), the hydrodynamic solar cell does not break parity by construction; parity is intrinsically broken by dissipation, setting the direction of the photocurrent. Therefore, Eckart streaming provides a novel mechanism for photocurrent (photovoltage) generation. Signatures of down-converted dc voltage generation by THz radiation have been measured in ultraclean 2DEGs [58–61].

One can define Reynolds numbers to estimate the strength $I^{(2)}/I_0$ of the nonlinearity. The Reynolds number Re_γ for this system can be defined as

$$\mathrm{Re}_\gamma \equiv \frac{\frac{1}{l}\int_0^l \overline{F_{\mathrm{conv},x}^{(2)}}}{\rho_e^{(0)}\gamma u_0} = \frac{I_0}{\rho_e^{(0)}h}\frac{1}{2l\gamma}\left[1 - \frac{2 - 2\cos 2kl}{\cosh 2\alpha l - \cos 2kl}\right], \tag{15}$$

which explicitly appears in Eq. (14). The viscous Reynolds number can be similarly defined such that $\mathrm{Re}_\nu = \frac{h^2}{r_d^2}\mathrm{Re}_\gamma$, where we approximate the viscous gradients to have length scale $L = h$ [see Eq. (4)]. The contribution from Re_ν is hidden within r_d; in the limit $r_d \gg h$, where viscous contributions dominate, Re_ν can be made manifest by perturbatively expanding Eq. (14) in h/r_d. Since $r_d \gg h$ for the experimental systems of interest, the Reynolds number $\mathrm{Re}_\gamma \sim I^{(2)}/I_0$ corresponds to the scale of dc current (up to a small viscous correction).

We now estimate the size the dc current in experiment (see Appendix A for dispersion relations). We take device size $l = 50\ \mu$m and $h = 5\ \mu$m and operate at $\omega = 1$ THz, with graphene-hBN parameters from Sec. II B; for these choices, the interference effects are small since $\alpha l \sim 5$. Therefore, we find $\mathrm{Re}_\gamma \sim I_0/(312\ \mathrm{mA})$ and therefore $\overline{I^{(2)}}/\mathrm{nA} \sim (I_0/24\ \mu\mathrm{A})^2$. Observing the oscillatory effects is more difficult, requiring smaller l and more measurement precision. Despite this, in an optimistically sized device of length $l = 20\ \mu$m, we plot the frequency dependence of Re_γ in Fig. 4. The oscillations are suppressed by a factor of 0.01; if one asks for a streaming current $\overline{I^{(2)}} \sim 1$ nA, the oscillations will be of order 10 pA. We therefore conclude that an Eckart streaming current should be visible in current experiments, with interference oscillations being a challenging observable.

V. RAYLEIGH STREAMING

We now turn to the limit where boundary dissipation dominates, i.e., the bulk dissipation α is negligible. Here, the no-slip condition is critical. In a rectangular back-gated device of width h [see Fig. 1(c)], we consider setting up a longitudinal standing wave of wavelength $\lambda \gg \alpha^{-1}$ along x. In this case, the system cannot support a finite dc current due to reflection symmetry in y. Therefore, down-converted dc current flows sourced by the convective force [see Eq. (3)] must circulate. The circulating current leads to a measurable orbital magnetization of wavelength $\lambda/2$ along x with reflection-symmetric modulation along y [see Fig. 1(c)]. This is the analog of Rayleigh streaming in classical hydrodynamics, where the convective force is primarily generated by boundary dissipation [51,52,62]. Remarkably, localized boundary effects lead to nontrivial flows throughout the bulk (see Appendix D for full mathematical details).

A. Perturbative calculation

We begin by working perturbatively in the input current amplitude u_0, where at linear order we take the longitudinal wave ansatz

$$v_{l,x}^{(1)} = u_0 \sin kx \cos \omega t. \tag{16}$$

This is consistent with a current-fixed boundary condition $J_x(x = 0) = 0$ (i.e., dc current $\bar{I} = 0$). For simplicity, we work in a semi-infinite strip of width h (i.e., $|y| \leqslant h/2$ and $x \geqslant 0$) with the above current-fixed boundary condition. To satisfy no-slip, a transverse mode $\mathbf{v}_t^{(1)}$ is necessary to correct the total flow $\mathbf{v}^{(1)} = \mathbf{v}_l^{(1)} + \mathbf{v}_t^{(1)}$. This transverse correction disperses along y with wave number $k_t = k_t' + ik_t''$, and hence forms a "boundary layer" of size $1/k_t''$ exponentially localized to the wall. We will work in the thin boundary layer and long-wavelength limit $k_t''^{-1} \ll h \ll \lambda$. In this limit, the resulting convective force [see Eq. (3)] can be schematically written as

$$\overline{F_{\mathrm{conv},x}^{(2)}} \sim \rho^{(0)}u_0^2 k\, e^{-k_t''y_+}\sin 2kx + (y \leftrightarrow -y), \tag{17}$$

where $y_+ = y + \frac{h}{2}$ is the distance from the lower boundary [63]. As a result of the quadratic nonlinearity, the wavelength of the convective force is halved to $\lambda/2$. In addition, the convective force is localized to the boundary layer, reflecting the fact that convection is driven by boundary dissipation. It is therefore convenient to divide the flow into bulk and boundary-layer regions, stitched together at the interface. Despite the localized nature of the convective force, its effect will persist into the bulk by providing a slip boundary condition.

Now, we study the second-order dc flow. We first consider the boundary-layer region, assuming that the viscous length scale $r_d \equiv \frac{\nu}{\gamma} \ll h$. The convective force localized to the boundary layer of size $1/k_t''$ leads to a localized flow along x. Because of the shear viscosity ν, the boundary-layer momentum propagates into the bulk with the viscous length scale r_d. Therefore, the boundary layer "screens" the no-slip condition, providing instead a slip velocity for the bulk flow. This slip velocity can be written as $v_{\mathrm{slip}}^{(2)}\sin 2kx$, where schematically $v_{\mathrm{slip}}^{(2)} \sim \frac{u_0^2 k}{4\gamma}e^{-1/k_t''r_d}$. Equipped with the slip boundary, we now solve the NS equation [Eq. (2)] for the bulk flow where the convective force vanishes, and we obtain

$$\overline{J_{\mathrm{bulk},x}^{(2)}} = J_{\mathrm{slip}}^{(2)}\sin 2kx\left[\frac{\frac{h}{2r_d}\cosh\frac{y}{r_d} - \sinh\frac{h}{2r_d}}{\frac{h}{2r_d}\cosh\frac{h}{2r_d} - \sinh\frac{h}{2r_d}}\right], \tag{18}$$

$$\overline{J_{\mathrm{bulk},y}^{(2)}} = J_{\mathrm{slip}}^{(2)}2kr_d\cos 2kx\left[\frac{-\frac{h}{2r_d}\sinh\frac{y}{2r_d} + \frac{y}{r_d}\sinh\frac{h}{2r_d}}{\frac{h}{2r_d}\cosh\frac{h}{2r_d} - \sinh\frac{h}{2r_d}}\right]. \tag{19}$$

The slip current $J_{\mathrm{slip}}^{(2)} \equiv \rho_e^{(0)}v_{\mathrm{slip}}^{(2)}$ results from boundary convection, while the term in brackets is a geometric factor resulting from satisfying the slip velocity boundary condition. The dc current flow is plotted in Fig. 1(c), where it is clear that the current circulates in cells of length $\lambda/4$ and width $h/2$.

B. Discussion and estimates

A previous related proposal by Dyakonov and Shur [57] and its recent extension [39] discussed down-conversion effects with a current-fixed boundary $J(x = 0) = 0$, similar to this case. However, they instead took a stress-free boundary condition that has no boundary dissipation. In their case, there is no circulating current; without boundary-layer contributions, the convective force only leads to an excess of dc voltage (see Appendix D). Therefore, Rayleigh streaming
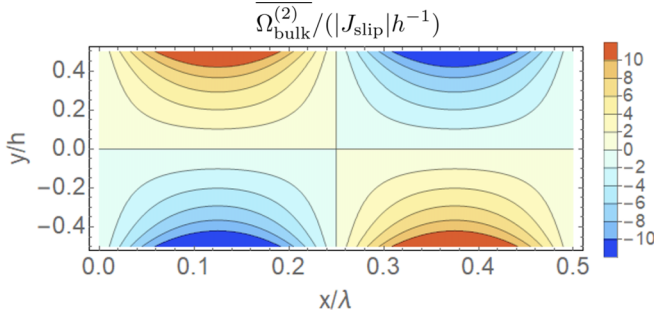
FIG. 5. A plot of the bulk vorticity distribution $\overline{\Omega^{(2)}_{\text{bulk}}} \equiv \nabla \times \overline{\mathbf{J}^{(2)}_{\text{bulk}}}$ induced by Rayleigh streaming for $h = 5\ \mu\text{m}$ and $\omega = 2$ THz with graphene-hBN parameters as in Sec. II B. The local bulk vorticity corresponds to a Coulomb-like point source of magnetic field due to Ampere's law.

is qualitatively distinct from previous nonlinear proposals in electron hydrodynamics.

Since the effect of the convective force is to generate a slip velocity $v^{(2)}_{\text{slip}}$, we can estimate the scale $v^{(2)}_{\text{slip}}/u_0$ by an appropriate Reynolds number. The Reynolds number Re_γ is defined in this case to be

$$\text{Re}_\gamma \equiv \frac{\max \overline{F^{(2)}_{\text{conv}}}}{\rho^{(0)} \gamma u_0} = \frac{I_0}{\rho^{(0)}_e h} \frac{k}{4\gamma} f(\omega/\gamma), \qquad (20)$$

where f is a dimensionless function of ω/γ described in Appendix D [64]. We remark that f develops an interesting resonance at $\omega = \frac{\sqrt{5}}{2}\gamma$ where perturbation theory breaks down, but we operate away from this point and will not discuss it further. It turns out $\text{Re}_\gamma\, e^{-1/k''_t r_d} = v^{(2)}_{\text{slip}}/u_0$, i.e., slip velocity is given by the Reynolds number up to an exponential factor controlled by the viscous length scale r_d. However, the viscous Reynolds number Re_ν does not contribute to the effect; in the limit $\gamma \to 0$, the scale $v^{(2)}_{\text{slip}}/u_0$ is instead set by the Mach number $u_0 k/\omega$. Despite the necessity of a finite shear viscosity ν to generate a convective force, Re_ν does not set the scale $v^{(2)}_{\text{slip}}$ of the result; this curious fact was first remarked by Rayleigh [65] (see Appendix D for additional discussion).

We propose that the circulating flow profile could be detected via magnetometry. To estimate the effect in realistic systems, we set $\omega = 2$ THz and channel width $h = 5\ \mu\text{m}$ with graphene-hBN parameters as in Sec. II B (see Appendix A for dispersion relations). We first verify the assumptions we made: $k''^{-1}_t \ll h \ll \lambda$, $r_d \ll h$, and $\alpha \ll k$. These are $k''_t h \sim 13$, $h/\lambda \sim 0.80$, $r_d/h \sim 0.08$, and $\alpha/k \sim 0.2$, so we expect our solution to be roughly correct. For the scale of the dc effect, we find $\text{Re}_\gamma \sim I_0/(23 \text{ mA})$ and $k''_t r_d \sim 1.1$, so that $v_{\text{slip}} \sim (I_0/71 \text{ mA}) u_0$. Since Ampere's law implies $-\nabla^2 B_z = \mu_0 \nabla \times \mathbf{J} \delta(z)$, the vorticity $\Omega \equiv \nabla \times \mathbf{J}$ acts as a Coulomb-like point source of magnetic field. The vorticity is plotted for these parameters in Fig. 5, where it is concentrated near the edges since the viscous length scale $r_d \ll h$ is small. To make a rough estimate of the magnetic field strength, we take $\overline{B_z} \sim \frac{\mu_0}{z} \int_{\text{cell}} \nabla \times \overline{\Omega^{(2)}_{\text{bulk}}}$ at a height z from the sample; we approximate the magnetic field to be sourced by the net circulation in the nearest vortical cell. This gives $B_z \sim \frac{(I_0/9.3\mu\text{A})^2}{z/\mu\text{m}} \times 10^{-10}$ T.

Therefore, the magnetic fields should be detectable for $I_0 \sim 9.3\ \mu\text{A}$ by scanning SQUID magnetometers.

VI. SUMMARY AND OUTLOOK

This paper argues for using nonlinear dc transport and other manifestations of convective nonlinearity to identify and study electron hydrodynamics. We have laid out three electronic analogs of nonlinear classical phenomena—the Bernoulli effect, Eckart streaming, and Rayleigh streaming—which lead to an experimentally measurable nonlinear *I-V* characteristic, down-converted dc current, and dc current vortices, respectively (see Fig. 1). We have opted to derive and discuss all three effects using the familiar Navier-Stokes formalism, leaving a more complete microscopic treatment for future work. All three effects result from the interplay of the nondissipative and nonlinear convection force with other dissipative contributions in Navier-Stokes from viscosity and momentum relaxation. As the convection force is a nondissipative term that couples nearby velocity fields, it seems unlikely that such a term could arise without electron-electron interactions. Therefore, we believe such proposals provide strong evidence for the emergence of a hydrodynamic regime.

It is interesting to note that interactions do not play an explicit role in our results—both convection and momentum relaxation (the dominant form of relaxation) are well understood in the noninteracting limit of the many-electron problem. Instead, strong electron-electron interactions justify the coarse-grained effective description, removing the need to consider the complications of quasiparticle physics. In particular, local equilibration (assumed throughout) is likely to be violated in the limit of weak interactions, requiring a more systematic microscopic treatment. This will be required, for example, before extrapolating our results to low temperatures.

To obtain stronger nonlinear signatures, one would like to make the Reynolds numbers Re_ν and Re_γ as large as possible. Since the viscous length scale $r^2_d = \nu/\gamma$ is typically smaller than the characteristic lengths in experiment, Re_γ is the limiting factor. In addition to reducing the momentum relaxation rate γ, one could also reduce the density n at fixed current to improve the Reynolds numbers; particles must move more rapidly to maintain the current. Therefore, nonlinear effects should be most prominent in clean, low-density hydrodynamic materials. Our focus has been away from linear response, which is a bedrock foundation of experimental condensed-matter physics. Nonlinear phenomena are comparatively more difficult to interpret and tend to be less explored, especially with the purpose of extracting basic information, e.g., where in the phase diagram a given material happens to be. However, since our primary focus has been on *leading* deviations from linear response, we are nonetheless optimistic that identifying electron hydrodynamics from nonlinear behavior is feasible.

In particular, the detection of the ac-generated static current described above would provide strong evidence for the presence of hydrodynamic behavior. Additionally, hydrodynamic nonlinearities should also generate up-converted $2f$ signals, which we leave to future work. This also tantalizingly suggests the possible utility of hydrodynamic materials as a novel platform for creating nonlinear electronic devices [38,57].

The nonlinear *I*-*V* characteristic of the Venturi wedge device clearly displays the onset of instability phenomena far separated from linear response. Such convective instabilities are a known route to classical turbulence [48,49], i.e., in the absence of momentum relaxation. In the electronic system, where momentum relaxation dominates and viscous length scale r_d is short, we suspect that the behavior may be qualitatively distinct from turbulence. Band-structure modifications to the Navier-Stokes equations, such as a density and flow-dependent hydrodynamic mass [32–34], and heating effects going beyond our equation-of-state approximations can also give rise to novel nonlinear effects, which we leave to future work. These and other nonlinear phenomena [66–68] pose a fertile frontier for near-term exploration of electron hydrodynamics.

ACKNOWLEDGMENTS

APPENDIX A: OSCILLATORY HYDRODYNAMIC MODES

Here we study the hydrodynamic modes at linear order (without boundary conditions), where the convective term $\mathbf{F}_{\text{conv}}$ is neglected. Because of linearity, the harmonic modes will not mix; the linear-order ansatz $\mathbf{v}^{(1)} \propto e^{i(kx-\omega t)}$ is appropriate. We eliminate the variables p and ϕ in Navier-Stokes [Eq. (2)] by using density continuity [Eq. (1)] as well as the equations of state [Eqs. (6) and (7)]. The resulting dispersion relation can be separated in longitudinal ($\nabla \times \mathbf{v}^{(1)} = \mathbf{0}$) and transverse ($\nabla \cdot \mathbf{v}^{(1)} = \mathbf{0}$) contributions, which are given by

$$\omega_l^2 = \left(s_0^2 - i\omega_l[2\nu + \tilde{\zeta}]\right)k_l^2 - i\omega_l\gamma, \tag{A1}$$

$$\omega_t = i\nu k_t^2 - i\gamma, \tag{A2}$$

where $s_0^2 = s_{\text{FL}}^2 + s_{\text{cap}}^2$. The longitudinal dispersion describes a damped sound wave with undamped speed s_0; both pressure and electric forces contribute additively to s_0 as a result of the equations of state. In particular, the electronic contribution relies on backgate screening of the Coulomb interaction to achieve this form. The transverse dispersion describes the propagation of incompressible shear oscillations, whose spatial extent is controlled by the viscous length scale r_d; a finite shear viscosity is necessary for the transfer of momentum into adjacent layers. In contrast to the longitudinal case, the transverse modes do not drive density oscillations and therefore do not generate pressure or electric forces. Therefore, the transverse result is independent of the equations of state, and in particular it does not depend on the presence of a backgate.

We remark that measuring the attenuation of longitudinal and transverse oscillations would provide direct, boundary-independent measures of both shear and bulk viscosity, as opposed to dc flow profiles, which require the boundary [20–22]

or inhomogeneous current injection profiles [18,25] to enforce velocity gradients. A careful experimental study of finite-frequency behavior of hydrodynamic materials has yet to be done even at linear order, as far as the authors are aware; in particular, this could provide new cross-checks of previous viscosity measurements. A proposal for a shear viscometer utilizing oscillatory motion was made in Ref. [69].

APPENDIX B: ELECTRONIC VENTURI EFFECT—TREATING VISCOSITY

The full problem, with both finite (kinematic) shear viscosity ν and momentum relaxation γ, is challenging. Because viscous effects are controlled by a length scale $r_d = \sqrt{\frac{\nu}{\gamma}}$, one expects a crossover from viscous-dominated to relaxation-dominated flow as a function of local channel width $h = r\theta_0$. In particular, the resistance of the thin $h \ll r_d$ region should scale as $1/h^2$ (Gurzhi/Poiseuille regime), while the resistance of the $h \gg r_d$ region should scale as $1/h$ (Ohmic regime). Even in the viscous-dominated regime $\gamma \to 0$, a radial flow assumption is inconsistent with the fixed-voltage boundary conditions as described in the main text; angular components of velocity must contribute. Therefore, for finite ν we expect the exact solution of Eq. (9) to also break down for strong particle flows in the convergent direction, possibly toward turbulence.

Purely viscous limit—Jeffrey-Hamel flow

In the purely viscous limit $\gamma \to 0$, the leading-order flow is a generalization of Poiseuille flow to nonparallel walls. This case also admits an exact solution of the Navier-Stokes equation, known as Jeffrey-Hamel flow [48,49,70]. However, as we are only interested in low-velocity flows, a perturbative treatment will suffice. In contrast to fixed-voltage boundary conditions, where one cannot assume purely radial flow, making it more difficult to solve, we will assume fixed-current boundary conditions where the θ-dependent radial flow $\mathbf{v} = v_r(\theta)\hat{r}$ is a good ansatz. In addition, we take the divergence-free (incompressible) ansatz $v_r^{(1)} = F(\theta)/r$ for an as yet undetermined function F. Upon substitution and integration of the $\hat{\theta}$ NS equation [Eq. (2)], we find that the NS equations give

$$\frac{e}{m}\frac{\partial \phi^{(1)}}{\partial r} = \frac{\nu}{r^3}\frac{d^2F}{d\theta^2}, \tag{B1}$$

$$\frac{e}{m}\phi^{(1)} = \frac{2\nu}{r^2}F(\theta) + S(r), \tag{B2}$$

where $S(r)$ is determined from the boundary conditions. Substituting for $\phi^{(1)}$, we find that $S(r) = K\frac{\nu}{2r^2} + \text{const}$ for some constant K by separation of variables. The leading-order solution is

$$v_r^{(1)} = \frac{I}{ne}\frac{1}{r}\frac{1}{\tan\theta_0 - \theta_0}\left(\frac{\cos 2\theta}{\cos\theta_0} - 1\right), \tag{B3}$$

$$\frac{e}{m}\phi^{(1)} = \frac{I}{ne}\frac{2\nu}{r^2}\frac{1}{\tan\theta_0 - \theta_0}\frac{\cos 2\theta}{\cos\theta_0}. \tag{B4}$$

Since $v_r^{(2)} = 0$, the pressure gradient must balance the convective force. Therefore, the total potential is given by

$$\frac{e}{m}\phi = \frac{\nu I}{ne}\frac{1}{r^2}\frac{1}{\tan\theta_0 - \theta_0}$$
$$\times \left[\frac{\cos 2\theta}{\cos\theta_0} + \frac{I}{2ne\nu}\frac{1}{\tan\theta_0 - \theta_0}\left(\frac{\cos 2\theta}{\cos\theta_0} - 1\right)^2\right].$$
(B5)

We see that $\phi^{(2)}$ is suppressed by a viscous Reynolds number $\mathrm{Re}_\nu \sim \frac{I}{ne\nu}$, as expected. Analogous to the purely Ohmic case discussed in the main text, it is known that divergent Jeffrey-Hamel flow is unstable toward turbulence [48,49].

APPENDIX C: ECKART STREAMING

In this Appendix, we lay out the mathematical calculation of Sec. IV in full detail.

1. Leading-order solution

As mentioned in the main text, we take the ansatz that the leading-order solution is described by a longitudinal sound mode with wave vector $k_l = k + i\alpha$ [see Eq. (A1)]. Applying the voltage-fixed boundary conditions and using the density continuity equation [see Eq. (1)], we find

$$\phi^{(1)} = V_0\mathrm{Re}\left[\frac{e^{(ik-\alpha)x} - e^{(ik-\alpha)(2l-x)}}{1 - e^{(ik-\alpha)2l}}e^{-i\omega t}\right], \quad (C1)$$

$$v_x^{(1)} = u_0\mathrm{Re}\left[\frac{e^{(ik-\alpha)x} + e^{(ik-\alpha)(2l-x)}}{1 - e^{(ik-\alpha)2l}}e^{-i\arg k_l}e^{-i\omega t}\right], \quad (C2)$$

where $u_0 = \frac{CV_0}{\rho_e^{(0)}}\frac{\omega}{|k_l|}$, and Re denotes the real part. To satisfy the no-slip boundary, we must also include a divergence-free (incompressible) contribution to the flow corresponding to a boundary-layer correction, as is done in Sec. V. We defer the discussion of this correction to the end of this section, assuming that its contribution is small.

2. Second-order density continuity equation

We now turn to the time-averaged second-order hydrodynamic equations, where we have assumed $\overline{v_y^{(2)}} = 0$. The density continuity (i.e., current conservation) equation [see Eq. (1)] gives

$$\frac{\partial \overline{J_x^{(2)}}}{\partial x} \equiv \frac{\partial}{\partial x}\left[\rho_e^{(0)}\overline{v_x^{(2)}} + \overline{\rho_e^{(1)}v_x^{(1)}}\right] = 0, \quad (C3)$$

which tells us that $\overline{J_x^{(2)}}(y)$ only depends on y. We remark that it is crucial that $\overline{\mathbf{v}^{(2)}}$ is *not* divergence-free (incompressible); because the "drift" contribution $\overline{\rho_e^{(1)}v_x^{(1)}}$ is nonzero and x-dependent, divergenceful (compressive) contributions of $v_x^{(2)}$ are necessary to satisfy current conservation.

3. Second-order Navier-Stokes equation—dc forces and screening

Replacing $\overline{v_x^{(2)}}$ in favor of $\overline{J_x^{(2)}}$ in the Navier-Stokes equation [see Eq. (2)], we get

$$\frac{m}{e}\left[-\nu\frac{\partial^2}{\partial y^2} + \gamma\right]\overline{J_x^{(2)}} = \overline{F_{\mathrm{eff}}^{(2)}}, \quad (C4)$$

$$-\rho_e^{(0)}\frac{\partial\overline{\phi_{\mathrm{eff}}^{(2)}}}{\partial x} + \overline{F_{\mathrm{conv},x}^{(2)}} + \overline{F_{\mathrm{elec},x}^{(2)}} + \overline{F_{\mathrm{comp},x}^{(2)}} \equiv \overline{F_{\mathrm{eff}}^{(2)}}, \quad (C5)$$

where we used a separation of variables with constant $\overline{F_{\mathrm{eff}}}$ to split the momentum equation, and $\rho_e^{(0)}\phi_{\mathrm{eff}}^{(2)} \equiv \rho_e^{(0)}\phi^{(2)} + p^{(2)}$. We remark that Eq. (C4) is an Ohmic-Poiseuille equation [12] describing steady, divergence-free (incompressible) flow in a rectangular channel, where $\overline{F_{\mathrm{eff}}}$ can be interpreted as the effective force driving the flow. The convective force is defined in Eq. (3), while the terms $\overline{F_{\mathrm{elec},x}^{(2)}}$ and $\overline{F_{\mathrm{comp},x}^{(2)}}$ are given by

$$\overline{F_{\mathrm{elec},x}^{(2)}} = \overline{\rho_e^{(1)}\frac{\partial\phi^{(1)}}{\partial x}}, \quad (C6)$$

$$\overline{F_{\mathrm{comp},x}^{(2)}} = (2\nu + \tilde{\zeta})\left[\overline{\rho^{(1)}\frac{\partial^2 v_x^{(1)}}{\partial x^2}} - \overline{\frac{\partial^2(\rho^{(1)}v_x^{(1)})}{\partial x^2}}\right], \quad (C7)$$

where in the second line we have used $\frac{\partial}{\partial x}\overline{(\rho^{(0)}v_x^{(2)})} = -\frac{\partial}{\partial x}\overline{(\rho^{(1)}v_x^{(1)})}$. These provide nonlinear contributions to $\overline{F_{\mathrm{eff}}^{(2)}}$ in addition to the convective force. The first term comes from the backreaction of the electric force; we remark that the presence of this nonlinearity was also noted by Ref. [39]. The second term comes from compressive dissipation. By solving for $\phi_{\mathrm{eff}}^{(2)}$ with the zero-voltage boundary conditions, we find the simple result

$$\overline{F_{\mathrm{eff}}} = \frac{1}{l}\int_0^l dx\,\overline{F_{\mathrm{conv},x}^{(2)}} + \overline{F_{\mathrm{elec},x}^{(2)}} + \overline{F_{\mathrm{comp},x}^{(2)}} \quad (C8)$$

The action of the effective voltage is to "screen" all the forces via a spatial average, rendering the resulting effective force x-independent. We comment that $\frac{1}{l}\int_0^l dx\,\overline{F_{\mathrm{elec},x}^{(2)}} = \frac{CV_0^2}{4l}$ has no α or k dependence, and therefore no interference behavior; the value of $\overline{F_{\mathrm{elec},x}^{(2)}}$ is fixed at the ends by the voltage boundary conditions. By dimensional analysis, these contributions are small relative to the convective force when $\frac{s_{\mathrm{cap}}^2\omega^2}{|k_l|^2} \ll 1$ and $\frac{(2\nu+\tilde{\zeta})|k_l|^2}{\omega} \ll 1$, respectively. For parameters as discussed in the main text, we find that $\frac{s_{\mathrm{cap}}^2|k_l|^2}{\omega^2} \sim 0.24$ and $\frac{(2\nu+\tilde{\zeta})|k_l|^2}{\omega} \sim 0.06$ are small, so that ignoring $\overline{F_{\mathrm{elec},x}^{(2)}}$ and $\overline{F_{\mathrm{comp},x}^{(2)}}$ is valid.

4. Rectified dc solution

The solution of the Ohmic-Poiseuille equation [Eq. (C4)] is

$$\overline{J_x^{(2)}} = \rho_e^{(0)}u_0\left[\frac{\overline{F_{\mathrm{eff}}^{(2)}}}{\rho^{(0)}\gamma u_0}\right]\left(1 - \frac{\cosh\frac{y}{r_d}}{\cosh\frac{h}{2r_d}}\right), \quad (C9)$$

$$\overline{I^{(2)}} = I_0\left[\frac{\overline{F_{\mathrm{eff}}^{(2)}}}{\rho^{(0)}\gamma u_0}\right]\left(1 - \frac{2r_d}{h}\tanh\frac{h}{2r_d}\right). \quad (C10)$$

The term in square brackets is suggestively written to resemble momentum-relaxation Reynolds number Re_γ, which is indeed true when the convective force dominates [see Eq. (15)]. We remark that the convective contribution to $I^{(2)}/I_0$ is largely α-independent [see Eq. (14)]; in the limit $\alpha l \gg 1$, where the interference term can be neglected, the result is surprisingly α-independent even though α was necessary to generate convective gradients. Instead, the scale of the convective gradient is screened, being controlled by the device length l^{-1}. This α-independence has an analog in Rayleigh streaming, where the shear viscosity ν does not set the scale of the rectified bulk flow even though it was necessary to set up convective forces.

5. Revisiting boundary dissipation (Rayleigh streaming)

We return to the issue of the no-slip condition and boundary-layer corrections (i.e., Rayleigh streaming), which we ignored for the leading-order solution. For simplicity, we will neglect contributions from the reflected wave (i.e., $\alpha l \gg 1$). As discussed in Sec. V, boundary-layer corrections are described by the transverse mode $k_t = k_t' + i k_t''$, decaying exponentially from the wall with length $1/k_t''$. For parameters as discussed in the main text, we find $k_t'' h \sim 8.2 > 1$ so that it is a good assumption that the boundary layer is thin. Therefore, boundary dissipation (i.e., Rayleigh streaming) effects will lead to a nonzero slip velocity for the bulk flow also in the forward x-direction. Upon solving the Ohmic-Poiseuille equation [Eq. (C4)] with a voltage-fixed boundary condition $\phi(x = l) = 0$ (as in the main text), we get an additional contribution

$$\overline{J^{(2)}_{\mathrm{Rayleigh},x}} = v^{(2)}_{\mathrm{slip}} \frac{\cosh \frac{y}{r_d}}{\cosh \frac{h}{2r_d}}, \tag{C11}$$

$$\overline{I^{(2)}_{\mathrm{Rayleigh}}} = v^{(2)}_{\mathrm{slip}} \tanh \frac{h}{2r_d}. \tag{C12}$$

Therefore, the no-slip boundary (i.e., Rayleigh streaming) only provides a quantitative correction to the dc current. By estimating $v^{(2)}_{\mathrm{slip}} \sim u_0 e^{-1/k_t'' r_d} \frac{I_0 |k_l|}{\rho_e^{(0)} h \gamma}$ from the Rayleigh Reynolds number in Eq. (20) with exponential decay arising from the viscous length scale r_d, we find that boundary dissipation contributes additively to the bulk dissipation contribution.

If instead one takes the current-fixed boundary condition $J(x = l) = 0$, a rectified dc voltage will develop as discussed in previous works [39,57]. However, these previous works did not consider the effect of a no-slip boundary. As a result of no-slip, we expect only a quantitative change to the dc voltage analogous to the previous case. However, a qualitative change occurs in the current flow—a circulating current must develop in the channel as in Sec. V. The length and width of the circulation will be set by the device dimensions, as opposed to that of Sec. V where the length is set by the wavelength. Surprisingly, the bulk current density flows in an opposite direction to that of the convective force; because convective forces are stronger near the boundary than the bulk, the forward dc flow along x must be near the boundary while the counterflow is in the bulk [51]. This reversed bulk counterflow would also be interesting evidence for hydrodynamic behavior, though measuring the local current density may prove challenging.

APPENDIX D: RAYLEIGH STREAMING

In this Appendix, we fill out the mathematical details of Sec. V.

1. Leading-order solution—Boundary corrections

Recall that we work in the limit $k_t''^{-1} \ll h \ll \lambda$ of a thin boundary layer and long wavelength. In this limit, we can separate the flow into bulk and boundary regions, stitching the flow together at the interface. We first focus on the boundary-layer region, concentrating on the lower boundary layer near $y = -h/2$; flow at the upper boundary layer is given by reflection symmetry about $y = 0$. In the lower boundary layer, the leading-order longitudinal (irrotational) and transverse (incompressible) velocity components of $\mathbf{v}^{(1)}_{\mathrm{wall}}$ are

$$v^{(1)}_{\mathrm{wall},l,x} = v^{(1)}_{l,x} = u_0 \sin kx \, \mathrm{Re}\, e^{i\omega t}, \tag{D1}$$

$$v^{(1)}_{\mathrm{wall},t,x} = -u_0 \sin kx \, \mathrm{Re}\big[e^{ik_t y_+} e^{-i\omega t} \big], \tag{D2}$$

$$v^{(1)}_{\mathrm{wall},t,y} = -u_0 k \cos kx \, \mathrm{Re}\bigg[\big(1 - e^{ik_t y_+}\big) \frac{e^{-i\omega t}}{ik_t} \bigg], \tag{D3}$$

where $y_+ = y + \frac{h}{2}$ is the distance from the lower wall, we take $k_t'' > 0$, and Re denotes the real part. Although $v^{(1)}_{\mathrm{wall},y}$ is small compared to $v^{(1)}_{\mathrm{wall},x}$, the y-gradients of $v^{(1)}_{\mathrm{wall},y}$ are large and must be included when computing the convective force. The longitudinal contribution $v^{(1)}_{\mathrm{wall},l,x}$ is inherited from the longitudinal ansatz of Eq. (16). We remark that we have not assumed that $v^{(1)}_{\mathrm{wall}}$ is divergence-free (incompressible), unlike classic discussions [48,62,65]; that the divergence-free (incompressible) ansatz is not correct has been previously pointed out [51,71], though it has no consequence in the limit $\gamma \to 0$. In the limit $k_t'' y_+ \gg 1$, we find that $v_{\mathrm{wall},x}$ returns to our longitudinal ansatz $v^{(1)}_{l,x}$ as the boundary-layer corrections exponentially vanish. However, $v^{(1)}_{\mathrm{wall},t,y}$ is nonzero in this limit and requires correction in the bulk. We will not concern ourselves with the bulk corrections to $v^{(1)}_y$, as they are small and do not contribute substantially to the convective force [51].

Therefore, the convective force in the bulk and boundary layers is

$$\overline{F^{(2)}_{\mathrm{conv,\,bulk},x}} = \rho^{(0)} u_0^2 k \tfrac{1}{4} \sin 2kx (-2), \tag{D4}$$

$$\begin{aligned}
\overline{F^{(2)}_{\mathrm{conv,\,wall},x}} &= \rho^{(0)} u_0^2 k \tfrac{1}{4} \sin 2kx \\
&\times [-2 + (3 + e^{2i\theta_t}) e^{ik_t y_+} - 2e^{-2k_t'' y_+} \cos^2 \theta_t],
\end{aligned} \tag{D5}$$

where $\theta_t \equiv \arg k_t$.

2. Second-order Navier-Stokes

We now study the dc second-order flow. We begin by noting that the assumption $k_t''^{-1} \ll h \ll \lambda$ implies that $v_y \ll v_x$, i.e., flow is primarily along x because the channel is thin. By using the NS equations [Eq. (2)], this implies that the effective voltage $\phi_{\mathrm{eff}} = \phi + \frac{1}{\rho_e^{(0)}} p$ satisfies $\frac{\partial \phi_{\mathrm{eff}}}{\partial y} \ll \frac{\partial \phi_{\mathrm{eff}}}{\partial x}$, i.e., voltage gradients (and density gradients) are also primarily along x.

Next, we simplify the NS equation [Eq. (2)]. First, we note that the back-reactive electric force $\mathbf{F}_{\text{elec}}^{(2)} \equiv \overline{\rho_e^{(1)} \nabla \phi^{(1)}} = 0$. We will also assume that compressional dissipation $\mathbf{F}_{\text{comp}} \equiv (2\nu + \tilde{\zeta})\rho \nabla \nabla \cdot \mathbf{v}$ is negligible, which is consistent with our assumption that the longitudinal attenuation α is small. Finally, for simplicity we neglect the additional term $\nu \overline{\rho_e^{(1)} \nabla \times \nabla \times \mathbf{v}^{(1)}}$ as is done in classical treatments of Rayleigh streaming [48,51,62,65,71]; this term depends on the density dependence of ν, where classical works assumed that the dynamic viscosity $\mu \equiv \rho\nu$ is constant. Therefore, the NS equation becomes

$$\frac{m}{e}\left[-\nu\frac{\partial^2}{\partial y^2} + \gamma\right]\overline{J_x^{(2)}} = \overline{F_{\text{conv},x}^{(2)}} - \rho_e^{(0)}\frac{\partial\overline{\phi_{\text{eff}}^{(2)}}}{\partial x}, \qquad (D6)$$

where we have used $k_t''^{-1} \ll h \ll \lambda$ to drop the x-derivatives [cf. Eqs. (C4) and (C5)]. Note that this form is equivalent to assuming that $\mathbf{v}^{(2)}$ is divergence-free (incompressible).

Since the convective force is only x-dependent in the bulk, we must have

$$\rho_e^{(0)}\frac{\partial\overline{\phi_{\text{eff}}^{(2)}}}{\partial x} = \overline{F_{\text{conv,bulk},x}} \qquad (D7)$$

upon imposing $\bar{I} = 0$ [i.e., $J_x(x=0) = 0$]. More concretely, the boundary conditions for $\overline{v_x^{(2)}}(y = \pm h/2)$ will fix the y-dependent homogeneous solutions of Eq. (D6), leaving $\overline{\phi_{\text{eff}}^{(2)}}$ to enforce $\overline{I^{(2)}} = 0$. Since $\frac{\partial\overline{\phi_{\text{eff}}^{(2)}}}{\partial y}$ is small, this expression for $\phi_{\text{eff}}^{(2)}$ is also valid in the boundary layer. Therefore, after "screening" from the effective voltage, the resultant force is only nonzero in the boundary layer.

3. Second-order boundary-layer solution

We first solve Eq. (D6) in the boundary layer, where the "screened" convective force is not negligible. Assuming $r_d \ll h$, the solution for the lower boundary layer is

$$\overline{J_{\text{wall},x}^{(2)}} = \rho_e^{(0)}u_0\sin 2kx\,\text{Re}\left[\frac{v_{\text{slip}}}{u_0} - \frac{u_0 k}{4\gamma}\left(-\frac{(3 + e^{2i\theta_t})e^{ik_t y_+}}{k_t^2 r_d^2 + 1} - \frac{(2\cos^2\theta_t)e^{-2k_t'' y_+}}{4k_t''^2 r_d^2 - 1}\right)\right], \qquad (D8)$$

$$v_{\text{slip}}^{(2)} = \frac{u_0^2 k}{4\gamma}e^{-\frac{y_+}{r_d}}\text{Re}\left[-\frac{(3 + e^{2i\theta_t})(i\tilde{\omega} + 2)}{4 + \tilde{\omega}^2} - \frac{2\cos^2\theta_t}{-3 + 2\sqrt{1 + \tilde{\omega}^2}}\right], \qquad (D9)$$

where $v_{\text{slip}}^{(2)}$ enforces the no-slip boundary conditions, and we have rewritten $k_t^2 r_d^2$ in terms of $\tilde{\omega} = \omega/\gamma$ using Eq. (A2). Away from the wall where the convective force vanishes, the velocity $v_{\text{wall},x}^{(2)} \to v_{\text{slip}}^{(2)}\sin 2kx$ achieves a nonzero limiting value if $k_t'' r_d$ is sufficiently large; the boundary layer sets up a slip boundary for the bulk flow. In the main text, we (optimistically) approximate the size of the boundary to be $1/k_t''$ so that we evaluate $v_{\text{slip}}^{(2)}$ at $y_+/r_d = 1/(k_t'' r_d)$. The resulting bulk flow is solved from Eq. (D6) with a vanishing right-hand side and with the slip boundary generated from the boundary layer; the solution is given in the main text [Eqs. (18) and (19)].

We make three remarks on v_{slip}. First, in the limit $\nu \to 0$, the flow becomes increasingly singular at the walls so

the boundary layer will no longer by described by hydrodynamics. Second is the surprising fact that ν is largely ν-independent. In the limit $\gamma \to 0$, we recover the classical result $v_{\text{slip}} = -\frac{3u_0}{8}\frac{u_0 k}{\omega}$, which is ν-independent, despite the necessity of ν to set up convective gradients. Instead of the viscous Reynolds number Re_ν, the slip velocity is controlled by the Mach number $u_0\omega/k$. This was first noted by Rayleigh in the classical situation [65]. Finally, v_{slip} has a resonance at $\omega = \frac{\sqrt{5}}{2}\gamma$ corresponding to $-4k_t''^2 r_d^2 + 1 = 0$. We leave further study of this interesting convective instability to future work; for this paper, we only work in the limit $v_{\text{slip}} \ll u_0$ where perturbation theory is valid.

[1] K. Damle and S. Sachdev, Nonzero-temperature transport near quantum critical points, Phys. Rev. B **56**, 8714 (1997).

[2] D. T. Son and A. O. Starinets, Viscosity, black holes, and quantum field theory, Annu. Rev. Nucl. Part. Sci. **57**, 95 (2007).

[3] S. Sachdev and M. Müller, Quantum criticality and black holes, J. Phys.: Condens. Matter **21**, 164216 (2009).

[4] S. A. Hartnoll, P. K. Kovtun, M. Müller, and S. Sachdev, Theory of the nernst effect near quantum phase transitions in condensed matter and in dyonic black holes, Phys. Rev. B **76**, 144502 (2007).

[5] L. Fritz, J. Schmalian, M. Müller, and S. Sachdev, Quantum critical transport in clean graphene, Phys. Rev. B **78**, 085416 (2008).

[6] M. S. Foster and I. L. Aleiner, Slow imbalance relaxation and thermoelectric transport in graphene, Phys. Rev. B **79**, 085415 (2009).

[7] M. Müller, J. Schmalian, and L. Fritz, Graphene: A Nearly Perfect Fluid, Phys. Rev. Lett. **103**, 025301 (2009).

[8] R. A. Davison, K. Schalm, and J. Zaanen, Holographic duality and the resistivity of strange metals, Phys. Rev. B **89**, 245116 (2014).

[9] A. Lucas and S. Sachdev, Memory matrix theory of magnetotransport in strange metals, Phys. Rev. B **91**, 195122 (2015).

[10] A. Lucas and S. A. Hartnoll, Resistivity bound for hydrodynamic bad metals, Proc. Natl. Acad. Sci. USA **114**, 11344 (2017).

[11] J. Zaanen, Planckian dissipation, minimal viscosity and the transport in cuprate strange metals, SciPost Phys. **6**, 61 (2019).

[12] I. Torre, A. Tomadin, A. K. Geim, and M. Polini, Nonlocal transport and the hydrodynamic shear viscosity in graphene, Phys. Rev. B **92**, 165433 (2015).

[13] L. Levitov and G. Falkovich, Electron viscosity, current vortices and negative nonlocal resistance in graphene, Nat. Phys. **12**, 672 (2016).

[14] T. Holder, R. Queiroz, T. Scaffidi, N. Silberstein, A. Rozen, J. A. Sulpizio, L. Ella, S. Ilani, and A. Stern, Ballistic and hydrodynamic magnetotransport in narrow channels, Phys. Rev. B **100**, 245305 (2019).

[15] G. Varnavides, A. S. Jermyn, P. Anikeeva, C. Felser, and P. Narang, Electron hydrodynamics in anisotropic materials, Nat. Commun. **11**, 4710 (2020).

[16] M. Shavit, A. Shytov, and G. Falkovich, Freely Flowing Currents and Electric Field Expulsion in Viscous Electronics, Phys. Rev. Lett. **123**, 026801 (2019).

[17] J. Crossno, J. K. Shi, K. Wang, X. Liu, A. Harzheim, A. Lucas, S. Sachdev, P. Kim, T. Taniguchi, K. Watanabe, T. A. Ohki, and K. C. Fong, Observation of the dirac fluid and the breakdown of the wiedemann-franz law in graphene, Science **351**, 1058 (2016).

[18] D. A. Bandurin, I. Torre, R. K. Kumar, M. Ben Shalom, A. Tomadin, A. Principi, G. H. Auton, E. Khestanova, K. S. Novoselov, I. V. Grigorieva, L. A. Ponomarenko, A. K. Geim, and M. Polini, Negative local resistance caused by viscous electron backflow in graphene, Science **351**, 1055 (2016).

[19] R. Krishna Kumar, D. A. Bandurin, F. M. D. Pellegrino, Y. Cao, A. Principi, H. Guo, G. H. Auton, M. Ben Shalom, L. A. Ponomarenko, G. Falkovich, K. Watanabe, T. Taniguchi, I. V. Grigorieva, L. S. Levitov, M. Polini, and A. K. Geim, Superballistic flow of viscous electron fluid through graphene constrictions, Nat. Phys. **13**, 1182 (2017).

[20] M. J. H. Ku, T. X. Zhou, Q. Li, Y. J. Shin, J. K. Shi, C. Burch, L. E. Anderson, A. T. Pierce, Y. Xie, A. Hamo, U. Vool, H. Zhang, F. Casola, T. Taniguchi, K. Watanabe, M. M. Fogler, P. Kim, A. Yacoby, and R. L. Walsworth, Imaging viscous flow of the dirac fluid in graphene, Nature (London) **583**, 537 (2020).

[21] J. A. Sulpizio, L. Ella, A. Rozen, J. Birkbeck, D. J. Perello, D. Dutta, M. Ben-Shalom, T. Taniguchi, K. Watanabe, T. Holder, R. Queiroz, A. Principi, A. Stern, T. Scaffidi, A. K. Geim, and S. Ilani, Visualizing poiseuille flow of hydrodynamic electrons, Nature (London) **576**, 75 (2019).

[22] P. J. W. Moll, P. Kushwaha, N. Nandi, B. Schmidt, and A. P. Mackenzie, Evidence for hydrodynamic electron flow in PDCOO2, Science **351**, 1061 (2016).

[23] J. Gooth, F. Menges, N. Kumar, V. Süb, C. Shekhar, Y. Sun, U. Drechsler, R. Zierold, C. Felser, and B. Gotsmann, Thermal and electrical signatures of a hydrodynamic electron fluid in tungsten diphosphide, Nat. Commun. **9**, 4093 (2018).

[24] G. M. Gusev, A. D. Levin, E. V. Levinson, and A. K. Bakarov, Viscous electron flow in mesoscopic two-dimensional electron gas, AIP Adv. **8**, 025318 (2018).

[25] A. D. Levin, G. M. Gusev, E. V. Levinson, Z. D. Kvon, and A. K. Bakarov, Vorticity-induced negative nonlocal resistance in a viscous two-dimensional electron system, Phys. Rev. B **97**, 245308 (2018).

[26] G. M. Gusev, A. S. Jaroshevich, A. D. Levin, Z. D. Kvon, and A. K. Bakarov, Stokes flow around an obstacle in viscous two-dimensional electron liquid, Sci. Rep. **10**, 7860 (2020).

[27] F. M. D. Pellegrino, I. Torre, A. K. Geim, and M. Polini, Electron hydrodynamics dilemma: Whirlpools or no whirlpools, Phys. Rev. B **94**, 155414 (2016).

[28] A. Shytov, J. F. Kong, G. Falkovich, and L. Levitov, Particle Collisions and Negative Nonlocal Response of Ballistic Electrons, Phys. Rev. Lett. **121**, 176805 (2018).

[29] A. Hui, S. Lederer, V. Oganesyan, and E.-A. Kim, Quantum aspects of hydrodynamic transport from weak electron-impurity scattering, Phys. Rev. B **101**, 121107(R) (2020).

[30] D. A. Bandurin, A. V. Shytov, L. S. Levitov, R. K. Kumar, A. I. Berdyugin, M. B. Shalom, I. V. Grigorieva, A. K. Geim, and G. Falkovich, Fluidity onset in graphene, Nat. Commun. **9**, 4533 (2018).

[31] A. Principi, D. Bandurin, H. Rostami, and M. Polini, Pseudo-euler equations from nonlinear optics: Plasmon-assisted photodetection beyond hydrodynamics, Phys. Rev. B **99**, 075410 (2019).

[32] D. Svintsov, V. Vyurkov, V. Ryzhii, and T. Otsuji, Hydrodynamic electron transport and nonlinear waves in graphene, Phys. Rev. B **88**, 245444 (2013).

[33] A. Tomadin and M. Polini, Theory of the plasma-wave photoresponse of a gated graphene sheet, Phys. Rev. B **88**, 205426 (2013).

[34] B. N. Narozhny, Electronic hydrodynamics in graphene, Ann. Phys. **411**, 167979 (2019).

[35] The curl is interpreted in 3D, so that it sends vectors to vectors.

[36] In our analysis, we follow the standard practice in electron hydrodynamics to ignore nonlinear fluctuation effects, such as long-time tails, which are known to be nonconvergent in low dimensions (including two) at finite temperature. While it is an interesting question to delineate conditions for such nonlinear regimes to be observable in electron fluids, we are not particularly optimistic in the present context, where disorder and low temperatures are of interest.

[37] The third dimensionless number which captures the relative strength of pressure (and potential) terms to convection turns out to be related to the Mach number.

[38] M. Dyakonov and M. Shur, Shallow Water Analogy for a Ballistic Field Effect Transistor: New Mechanism of Plasma Wave Generation by Dc Current, Phys. Rev. Lett. **71**, 2465 (1993).

[39] I. Torre, A. Tomadin, R. Krahne, V. Pellegrini, and M. Polini, Electrical plasmon detection in graphene waveguides, Phys. Rev. B **91**, 081402(R) (2015).

[40] A. Lucas and K. C. Fong, Hydrodynamics of electrons in graphene, J. Phys.: Condens. Matter **30**, 053001 (2018).

[41] U. Briskot, M. Schütt, I. V. Gornyi, M. Titov, B. N. Narozhny, and A. D. Mirlin, Collision-dominated nonlinear hydrodynamics in graphene, Phys. Rev. B **92**, 115426 (2015).

[42] A. Laturia, M. L. Van de Put, and W. G. Vandenberghe, Dielectric properties of hexagonal boron nitride and transition metal dichalcogenides: from monolayer to bulk, npj 2D Mater. Appl. **2**, 6 (2018).

[43] L. D. Landau, Sov. Phys. JETP **3**, 920 (1957).

[44] N. W. Ashcroft and N. D. Mermin, *Solid State Physics*, HRW International eds. (Holt, Rinehart and Winston, Orlando, FL, 1976).

[45] Boundary conditions are effectively inconsequential without viscosity. One could just as well taken no-stress boundary conditions (while including viscosity as the shear viscosity force vanishes [16]). The Corbino geometry is therefore smoothly connected to the $\theta_0 \to 2\pi$ limit, as the Corbino geometry is equivalent to no-stress boundary condition.

[46] When the device is gated, including p is equivalent to renormalizing e/m. In the absence of gating, the long-range Coulomb interaction suppresses density fluctuations, so the pressure contribution is expected to be negligible.

[47] M. J. M. de Jong and L. W. Molenkamp, Hydrodynamic electron flow in high-mobility wires, Phys. Rev. B **51**, 13389 (1995).

[48] L. D. Landau and E. M. Lifshitz, *Fluid Mechanics:* (Elsevier Science, Amsterdam, 2013), Vol. 6.

[49] L. Rosenhead, *Laminar Boundary Layers: An Account of the Development, Structure, and Stability of Laminar Boundary Layers in Incompressible Fluids, Together with a Description of the Associated Experimental Techniques*, Dover Books on Engineering and Engineering Physics (Dover, New York, NY, 1988).

[50] C. Eckart, Vortices and streams caused by sound waves, Phys. Rev. **73**, 68 (1948).

[51] W. Le Mars Nyborg, 11–Acoustic Streaming, in *Properties of Polymers and Nonlinear Acoustics*, edited by W. P. Mason, Physical Acoustics (Academic, New York, NY, 1965), Vol. 2 pp. 265–331.

[52] S. J. Lighthill, Acoustic streaming, J. Sound Vib. **61**, 391 (1978).

[53] M. Wiklund, R. Green, and M. Ohlin, Acoustofluidics 14: Applications of acoustic streaming in microfluidic devices, Lab Chip **12**, 2438 (2012).

[54] This is effectively equivalent to taking stress-free boundary conditions at leading order; the choice of boundary condition only weakly modifies the final result [see Eq. (14) and the subsequent footnote on the viscous correction].

[55] This is the only effect of the no-slip BC. For stress-free boundary conditions, this correction will be equal to 1. The dc flow profile will be constant along y, which is equivalent to setting $\nu \to 0$ as there is no shear viscosity force.

[56] Because $I_0 = \rho_e^{(0)} h \frac{C V_0}{\rho_e^{(0)}} \frac{\omega}{|k_l|}$, perturbation theory will break down for sufficiently low ω. This happens when $\omega \ll \gamma$, i.e., when k_l is dominated by γ and tends to a constant.

[57] M. I. Dyakonov and M. S. Shur, Plasma wave electronics: novel terahertz devices using two dimensional electron fluid, IEEE Trans. Electron Dev. **43**, 1640 (1996).

[58] R. Tauk, F. Teppe, S. Boubanga, D. Coquillat, W. Knap, Y. M. Meziani, C. Gallon, F. Boeuf, T. Skotnicki, C. Fenouillet-Beranger, D. K. Maude, S. Rumyantsev, and M. S. Shur, Plasma wave detection of terahertz radiation by silicon field effects transistors: Responsivity and noise equivalent power, Appl. Phys. Lett. **89**, 253511 (2006).

[59] L. Vicarelli, M. S. Vitiello, D. Coquillat, A. Lombardo, A. C. Ferrari, W. Knap, M. Polini, V. Pellegrini, and A. Tredicucci, Graphene field-effect transistors as room-temperature terahertz detectors, Nat. Mater. **11**, 865 (2012).

[60] V. Giliberti, A. Di Gaspare, E. Giovine, M. Ortolani, L. Sorba, G. Biasiol, V. V. Popov, D. V. Fateev, and F. Evangelisti, Down-conversion of terahertz radiation due to intrinsic hydrodynamic nonlinearity of a two-dimensional electron plasma, Phys. Rev. B **91**, 165313 (2015).

[61] D. A. Bandurin, D. Svintsov, I. Gayduchenko, S. G. Xu, A. Principi, M. Moskotin, I. Tretyakov, D. Yagodkin, S. Zhukov, T. Taniguchi, K. Watanabe, I. V. Grigorieva, M. Polini, G. N. Goltsman, A. K. Geim, and G. Fedorov, Resonant terahertz detection using graphene plasmons, Nat. Commun. **9**, 5392 (2018).

[62] N. Riley, Steady streaming, Annu. Rev. Fluid Mech. **33**, 43 (2001).

[63] More precisely, this is a schematic form of the screened convective force with contributions from the effective voltage $\phi_{\text{eff}}^{(2)} = \phi^{(2)} + \frac{1}{\rho^{(0)}} p^{(2)}$.

[64] As before, we only consider the screened convective force in the above equation, equivalent to including boundary contributions only.

[65] L. Rayleigh, On the circulation of air observed in kundt's tubes, and on some allied acoustical problems, Philos. Trans. R. Soc. London **175**, 1 (1884).

[66] O. Furtmaier, M. Mendoza, I. Karlin, S. Succi, and H. J. Herrmann, Rayleigh-bénard instability in graphene, Phys. Rev. B **91**, 085401 (2015).

[67] R. C. V. Coelho, M. Mendoza, M. M. Doria, and H. J. Herrmann, Kelvin-helmholtz instability of the dirac fluid of charge carriers on graphene, Phys. Rev. B **96**, 184307 (2017).

[68] P. O. Sukhachov, E. V. Gorbar, and I. A. Shovkovy, Hydrodynamics in dirac semimetals: Convection impossible, arXiv:2103.15836.

[69] A. Tomadin, G. Vignale, and M. Polini, Corbino disk viscometer for 2d quantum electron liquids, Phys. Rev. Lett. **113**, 235901 (2014).

[70] K. Millsaps and K. Pohlhausen, Thermal Distributions in Jeffery-Hamel Flows Between Nonparallel Plane Walls, J. Aeronaut. Sci. **20**, 187 (1953).

[71] P. J. Westervelt, The theory of steady rotational flow generated by a sound field, J. Acoust. Soc. Am. **25**, 60 (1953).